Acta Crystallographica Section D
Biological Crystallography
ISSN 0907-4449

Near-atomic resolution structures of urate oxidase complexed with its substrate and analogues: the protonation state of the ligand

Laure Gabison,[a] Mohamed Chiadmi,[a] Mohamed El Hajji,[b] Bertrand Castro,[b] Nathalie Colloc'h[c] and Thierry Prangé[a]*

[a]Laboratoire de Cristallographie et RMN Biologiques, UMR 8015 CNRS, France, [b]Sanofi–Aventis Recherche et Développement, Rue du Professeur Joseph Blayac, 34184 Montpellier, France, and [c]CI-NAPS, UMR 6232–UCBN–CNRS, Centre Cyceron, Boulevard Henri Becquerel, 14074 Caen CEDEX, France

Correspondence e-mail: thierry.prange@univ-paris5.fr

Received 3 February 2010
Accepted 25 March 2010

PDB References: urate oxidase, complex with xanthine, 3l8w; complex with 8-nitroxanthine, 3ld4; complex with uric acid and chloride, 3l9g; complex with 8-thiouric acid, 3lbg.

Urate oxidase (uricase; EC 1.7.3.3; UOX) from *Aspergillus flavus* catalyzes the oxidation of uric acid in the presence of molecular oxygen to 5-hydroxyisourate in the degradation cascade of purines; intriguingly, catalysis proceeds using neither a metal ion (Fe, Cu *etc*.) nor a redox cofactor. UOX is a tetrameric enzyme with four active sites located at the interface of two subunits; its structure was refined at atomic resolution (1 Å) using new crystal data in the presence of xanthine and at near-atomic resolution (1.3–1.7 Å) in complexes with the natural substrate (urate) and two inhibitors: 8-nitroxanthine and 8-thiouric acid. Three new features of the structural and mechanistic behaviour of the enzyme were addressed. Firstly, the high resolution of the UOX–xanthine structure allowed the solution of an old structural problem at a contact zone within the tetramer; secondly, the protonation state of the substrate was determined from both a halochromic inhibitor complex (UOX–8-nitroxanthine) and from the H-atom distribution in the active site, using the structures of the UOX–xanthine and the UOX–uric acid complexes; and thirdly, it was possible to extend the general base system, characterized by the conserved catalytic triad Thr–Lys–His, to a large water network that is able to buffer and shuttle protons back and forth between the substrate and the peroxo hole along the reaction pathway.

1. Introduction

Oxidases and/or oxygenases (monooxygenases and dioxygenases) usually require a metal or a cofactor to overcome the spin-restriction rule that forbids the direct reaction of molecular oxygen with their substrates. However, there are classes of oxygenases and oxidases that proceed efficiently without a requirement for cofactors or metal ions. How these enzymes manage to allow triplet dioxygen to react with singlet organic substrates so easily remains an intriguing feature (for reviews, see Fetzner, 2002; Fetzner & Steiner, 2010). Urate oxidase (UOX) belongs to the class of cofactor-less oxidases and is functional as a homotetramer with an external size of 60 × 60 Å, enclosing a tunnel 50 Å in length and 12 Å in diameter (Fig. 1*a*). The four chains (or subunits), *A*, *B*, *C* and *D*, are assembled according to an internal 222 symmetry which leads to the formation of a large central tunnel of unknown function. Subunits *A*–*B* and *C*–*D* are assembled around the tunnel, while subunits *A*–*C* and *B*–*D* are assembled along the tunnel. The active site of UOX is located at the interfaces of subunits *A*–*B* (or *C*–*D*); UOX degrades uric acid using dioxygen

without the assistance of any metal or other cofactor (Fig. 1*b*). Recent results on the mechanism using oxygen-pressurized crystallography and cyanide inhibition (Colloc'h *et al.*, 2008; Gabison *et al.*, 2008) provided additional structural evidence for the initial mechanism proposed by Tipton and coworkers (Kahn & Tipton, 1997; Tipton, 2002; Imhoff *et al.*, 2003), who suggested the initial binding of urate monoanion (the substrate) immediately followed by deprotonation to yield the more highly reactive species urate dianion. Once complexed within the active site, the dianion has the lowest ionization potential (Altarsha *et al.*, 2009). A number of uric acid analogues, such as xanthine (XAN), 8-nitroxanthine (8NXN), 8-thiouric acid (8THIO) and 8-azaxanthine (8AZA), are competitive inhibitors with a high affinity for UOX; they are known to react in the primary step of the reaction, but owing to the lack of a carbonyl group at C(8) (Fig. 2) they lead to a nonproductive complex or 'cul-de-sac'. In order to unravel the mechanism, it becomes important to evaluate the true ionization state of the substrate at the beginning of the reaction, a feature that requires determination of the hydrogen distribution around the ligand.

A crystallization protocol was designed that led to the production of crystals of the UOX–xanthine complex that occasionally diffracted to much higher resolution (1 Å at ∼100 K) than all of the structures reported to date (Retailleau *et al.*, 2005; Gabison *et al.*, 2008). Four new structures obtained at atomic (or near-atomic) resolution were exploited to derive information about the H atoms in the active site. In addition, these structures, hereafter designated UOX–XAN, UOX–8NXN, UOX–8THIO and UOX–UA (the complex with uric acid), allowed the resolution of some chain disorders that had been observed at the interface of UOX subunit contacts.

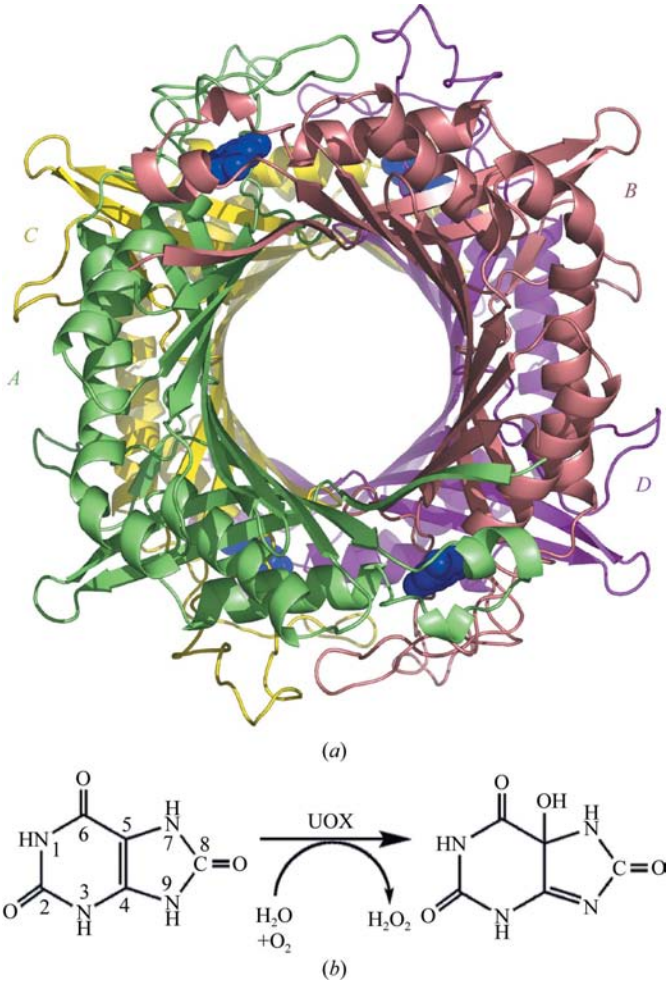

Figure 1
(*a*) The overall structure of the UOX homotetramer (coloured by chains); the four active sites are occupied by urate anions (shown in blue). (*b*) The catalyzed reaction leading to 5-hydroxyisourate (5-HIU). In solution 5-HIU spontaneously evolves to (±)-allantoin with a lifetime of about 20 min, while *in vivo* 5-HIU is rapidly degraded to (+)-allantoin by another enzymatic system (Ramazzina *et al.*, 2006).

2. Materials and methods

2.1. Inhibitors

Urate oxidase (UOX) from *Aspergillus flavus* is commercially produced under the brand name Fasturtec and was a gift from Sanofi–Aventis Co. The solution of UOX upon receipt was about 11 mg ml^{-1} in phosphate buffer. Prior to crystallization, the solution was exchanged against 0.05 *M* Tris buffer pH 8 and concentrated to 20 mg ml^{-1} according to optical density measurements. Uric acid and xanthine were purchased from Fluka Co.

8-Nitroxanthine (8NXN) was prepared according to a modification of the procedure of Mosselhi & Pfleiderer (1993): 2 g of xanthine were heated in a large excess of a 50:50 mixture of acetic acid and nitric acid under reflux and nitrogen flushing. After complete dissolution of the xanthine, a bright yellow precipitate gradually appeared. After 2 h and complete elimination of the red nitrogen dioxide, the mixture was ice-cooled and filtered and the precipitate was washed with 2 × 20 ml cold water. The 8-nitroxanthine powder (1.9 g) was dried under vacuum in the presence of potassium hydroxide pellets and was used without further purification.

8-Thiouric acid (8THIO) was prepared by the method of Loo *et al.* (1959). 1 g 5,6-diaminouracil (5 m*M*) and an excess of thiourea (13 m*M*) were heated for 1 h at 453–463 K. Once cooled, the mixture was dissolved in 10 ml 2 *M* NaOH and the

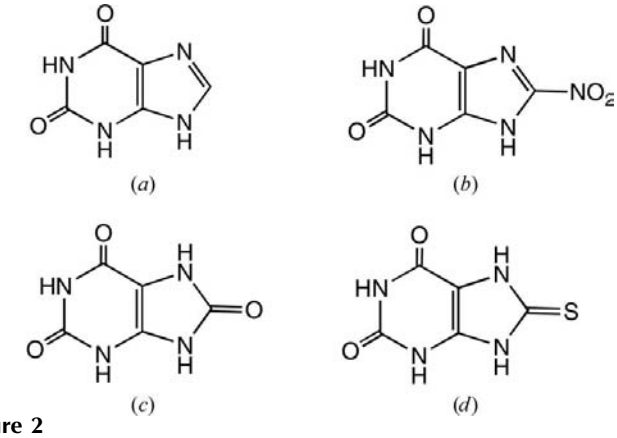

Figure 2
Structures of (*a*) xanthine (XAN), (*b*) 8-nitroxanthine (8NXN), (*c*) uric acid (UA) and (*d*) 8-thiouric acid (8THIO).

resulting solution was filtered on Norit charcoal and acidified using excess acetic acid. The precipitate of 8-thiouric acid was separated by centrifugation and recrystallized in acetic acid.

2.2. Crystallization

Crystals of the UOX complexes were obtained at 291 K (except for the UOX–XAN complex, which was obtained at 277 K) following the protocol previously reported by Retailleau *et al.* (2004) using solutions saturated with xanthine, 8-thiouric acid or 8-nitroxanthine at pH 8 in 0.05 *M* Tris buffer and 8% PEG 8000 as crystallizing agent (solution *A*) and protein solution at 20 mg ml^{-1} in the same Tris buffer (solution *B*). The batch method was used throughout, *i.e.* mixing the same amounts of solutions *A* and *B* in 100 µl wells. Once obtained, crystals were transferred to a cryoprotectant solution (solution *A* adjusted to 20% 2-methyl-2,4-pentanediol or ethylene glycol) for 2 min and then rapidly quenched and stored in liquid nitrogen.

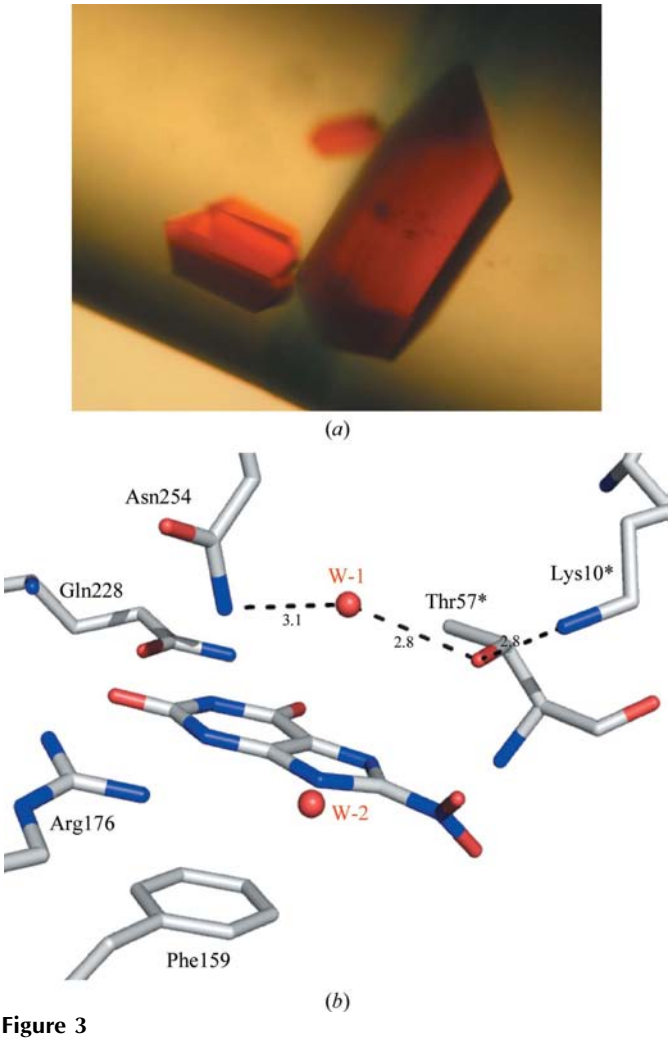

Figure 3
(*a*) Crystal of UOX–8-nitroxanthine used as a halochromic indicator. Upon binding, the bright yellow colour of 8-nitroxanthine at pH 8 changes to a deep red owing to the doubly deprotonated state of the ligand in the active site. (*b*) The 8-nitroxanthine ligand in the active site of urate oxidase as determined from the UOX–8NXN structure.

In the case of xanthine, an excess of α-(4-pyridyl-1-oxide)-*N*-*tert*-butylnitrone (4-POBN) was added to the initial solution to quench any free radicals that may be produced. Crystals of the UOX–XAN complex were obtained in 3 d at 277 K and grew to full size within a week.

In the case of 8-nitroxanthine, the bright yellow solution of 8NXN immediately gave rise to an orange colour upon mixing with the protein solution. This dramatic change in colour is attributed to a change in the ionization state of the ligand once complexed. Fig. 3(*a*) shows the resulting deep-red crystals of the UOX–8NXN complex.

In the case of 8-thiouric acid, large pale yellow–green crystals grew in a week.

In the case of uric acid (UA), when mixing solution *A* saturated with uric acid and solution *B* the reaction proceeds rapidly to the complete elimination of uric acid; the crystals obtained contain the end product of the complete reaction (allantoin) instead of the substrate (Gabison *et al.*, 2006). To complex uric acid in the structure, the reaction with oxygen must be inhibited by sodium cyanide (Gabison *et al.*, 2008) or conversely (as in this study) can be slowed using a concentrated solution of NaCl. The following procedure was used. A crystal of the 8-nitroxanthine complex (UOX–8NXN) was soaked in a solution saturated with uric acid (Tris buffer pH 8.0, 8% PEG 8000) plus ∼0.2 *M* NaCl. The ligand exchange was followed by the disappearance of the red colour of the crystal. When the exchange was complete (estimated as after about 5 min), the crystal was transferred into the cryoprotectant solution (∼20% 2-methyl-2,4-pentanediol) and immediately frozen.

2.3. Data collection

All data recordings were performed at the ESRF, Grenoble on beamlines BM14, BM16 or BM30 at 100 K. The same protocol was used for all crystals: 1° rotation per frame and a complete rotation of 120°. The crystal-to-detector distance was set according to the maximum resolution determined on a first test frame. In the case of the UOX–XAN structure a second 'low' resolution (∼1.9 Å) data set was recorded at a higher speed to obtain most of the reflections that are usually saturated at resolutions below 3 Å.

Data sets were processed using either the *HKL*-2000 suite (Otwinowski & Minor, 1997) or *MOSFLM* (Leslie, 1992) and were merged using the *CCP*4 package of programs (Collaborative Computational Project, Number 4, 1994). Results and data statistics are reported in Table 1.

2.4. Refinements

2.4.1. UOX–xanthine atomic resolution structure. The starting model was the urate oxidase structure (PDB code 2iba; Colloc'h *et al.*, 2007). The *SHELXL*/*SHELXH* program (Sheldrick, 2008) was used with individual isotropic constrained factors. Several rounds of (i) refinement, (ii) rebuilding on a graphics system, mostly in disordered side chains, and (iii) water-molecule location using the automated *ARP*/*wARP* procedure (Perrakis *et al.*, 2001) were conducted

Table 1
Data-collection and refinement statistics for the UOX–urate and UOX–inhibitor complexes.

All crystals belonged to space group *I*222 and all data were collected at 100 K. Values in parentheses are for the highest resolution bin. The wavelengths used were 0.946 Å (for the XAN complex; BM14 beamline), 0.979 Å (for the UA complex; BM16 beamline) and 0.982 Å (for the 8NXN and 8THIO complexes; BM30 beamline).

Ligand	Xanthine (XAN; Fig. 2*a*)	8-Nitroxanthine (8NXN; Fig. 2*b*)	Uric acid (UA; Fig. 2*c*)	8-Thiouric acid (8THIO; Fig. 2*d*)
Unit-cell parameters				
a (Å)	79.53	79.58	77.73	79.64
b (Å)	94.98	95.04	94.94	95.47
c (Å)	104.32	104.37	104.44	104.61
V (Å^3)	788001	789379	770848	795374
Resolution (Å)	29.4–1.0 (1.10–1.0)	29.4–1.35 (1.42–1.35)	23.9–1.75 (1.84–1.75)	39.8–1.50 (1.58–1.50)
No. of unique reflections	202546 (43833)	85931 (11863)	39308 (5601)	62477 (5922)
Redundancy	5.4 (3.7)	7.6 (4.5)	4.7 (4.1)	4.2 (3.8)
R_{merge} (%)	5.3 (20.1)	4.6 (16.4)	6.3 (20.1)	4.1 (8.6)
Completeness (%)	95.1 (84.1)	99.4 (99.4)	99.8 (99.0)	97.8 (96.1)
Mean $I/\sigma(I)$	9.6 (3.8)	25 (7.4)	31.5 (5.5)	29.4 (5.1)
Refinement				
No. of atoms in the model				
Protein	2359	2395	2358	2386
Ligand	11	14	12	2 × 12
Solvent				
H_2O	456	265	283	316
Na^+	1	1	1	1
Ethylene glycol	—	4	—	16
Other	14 [4-POBN]	—	1 [Cl^-]	8 [Tris]
Resolution range (Å)	29–1.0	25–1.35	10–1.75	25–1.50
No. of reflections used	202546	85679	39071	62332
No. of observed reflections [with $F > 4\sigma(F)$]	131827	80616	34994	60541
No. of parameters/No. of restraints	25827/31137	10727/9947	10643/9920	11017/9957
R_{work}, all reflections (%)	14.5	18.7	18.9	20.9
R_{work}, observed reflections (%)	12.0	18.2	18.4	20.6
R_{free} (%) [No. of reflections]	17.7 (9194)	22.5 (4305)	20.8 (1749)	24.1 (3233)
wR_2 on F^2 (%)	30.7	48.8	44.9	52.1
Mean standard deviations from ideality (target/value) [No.]				
1–2 distances (Å)	0.03/0.029 [2514]	0.034/0.028 [2466]	0.034/0.036 [2464]	0.034/0.034 [2489]
1–3 distances (Å)	0.087/0.085 [3374]	0.082/0.074 [3344]	0.082/0.078 [3340]	0.081/0.080 [3368]
Planes (Å)	0.43/0.41 [797]	0.43/0.39 [793]	0.43/0.38 [798]	0.43/0.39 [807]
Chiral zero volumes (Å^3)	0.08/0.08 [383]	0.10/0.06 [386]	0.10/0.06 [382]	0.10/0.05 [382]
Chiral nonzero volumes (Å^3)	0.080/0.085 [376]	0.10/0.07 [368]	0.10/0.05 [368]	0.10/0.07 [368]
Recalculated mean isotropic $\langle B \rangle$ factors (Å^2)				
Main-chain atoms	10.4	10.2	16.2	14.1
Side-chain atoms	13.7	14.4	19.8	17.4
Ligand	10.9	14.0	13.6	20.6
Water molecules	24.5	21.0	29.9	27.3
Other	25.8 [4-POBN]	40.0 [glycol]	—	24.1 [Tris], 38.0 [glycol]
Na^+	21.6	11.9	19.8	16.1
Cl^-	—	—	16.4	—
PDB code	3l8w	3ld4	3l9g	3lbg

at resolutions starting at 1.7 Å. The ligand (XAN) was manually placed in the active-site density. The resolution was then increased step by step up to the highest resolution available (1.0 Å). At the end of each round, the *R* factor was 22.5 (1.5 Å), 21.6 (1.3 Å) and 20.4 (1.15 Å) and its final value was 19.8%. As usual, water molecules were kept in the model when they met a number of chemical requirements such as correct bond angles and distances from polar atoms of both main-chain and side-chain atoms of UOX, as well as from other water molecules (the second shell of hydration), and also if their isotropic thermal factor did not exceed a value that was arbitrarily fixed at ∼60 Å^2 (or $U < 0.75$) during the refinement. A number of characteristic signatures in electron densities (one 4-POBN and one sodium ion) were also located and their contributions were added to the model.

In the second stage of refinement, anisotropic thermal parameters were gradually included at the highest resolution (1.0 Å) in blocks of ten in each cycle until completion (including water molecules), except for atoms in a 'free sphere' (with a radius of 7 Å) located around the active site, which were kept isotropic throughout.

H atoms were introduced in the model at their calculated positions using the HFIX command in *SHELXH*, but not in the 'free' sphere. At the end of these refinements, additional cycles of automated location of water molecules and/or ions using *ARP*/*wARP* were performed until completion and convergence. This procedure was adopted in order to avoid any unwanted extension of anisotropy vectors along the C—H direction that would flatten the density of unmodelled H atoms within the 'free' zone around the substrate.

At this stage, an $F_o - F_c$ map was calculated in the hope of deriving information about missing hydrogen contributions within the 'free sphere' (discussed later).

Finally, the refined model (reported in Table 1) was completed following additional rounds of refinement including atoms of the 'free sphere' as anisotropic atoms. The standard R_{free} was evaluated as 14.7% using 9194 randomly chosen structure factors. The model was validated against ideality of geometric parameters using standard tools (*PROCHECK* and *MolProbity*; Laskowski *et al.*, 1993; Chen *et al.*, 2010). At the end of refinement, the model comprised 2839 anisotropic atoms, 14 residues with disordered multi-position side chains (Lys4, Lys23, Lys114, Lys138, Lys171, Glu22, Glu41, Glu43, Glu213, Ser119, Ser199, Met231, Gln243 and Cys290) and about 15 water molecules showing double positions. The model also includes 2342 H atoms in theoretical positions and a molecule of the 4-POBN spin-trap molecule that emerged from $F_o - F_c$ maps and was located near the central channel. At the end of convergence, the R factors R (on F) and wR_2 (on F^2) were 12.0% and 30.7%, respectively.

2.4.2. UOX–uric acid, UOX–8-nitroxanthine and UOX–8-thiouric acid structures. Near-atomic resolution refinements started from the previously refined model of UOX–XAN at atomic resolution by removing ligands, ions and water molecules. Either the *CNS* (Brünger *et al.*, 1998) or *REFMAC* (Murshudov *et al.*, 1997) programs were initially employed using their specific application protocols. Atoms were refined with individual isotropic thermal factors using *SHELXL* (Sheldrick, 2008). Disordered side chains were kept in the model; water molecules, ions and ligands were introduced and refined. Finally, H atoms were placed at their calculated positions with an isotropic thermal factor riding on that of the bonded atom. Refinement parameters and statistics are also gathered in Table 1.

3. Results

UOX is an assembly of four subunits. Each monomer (*A*, *B*, *C* and *D*) features an antiparallel eight-stranded β-sheet with four helices located on the convex side of the β-sheet (Fig. 1*a*). The monomer is unstable and requires stabilization through oligomeric association. The *A*–*B* contact forms a 16-stranded β-barrel with helices forming the outside of the barrel. Two head-to-tail β-barrels build the full tetramer, which is crossed by a large central tunnel. There are three types of interface: the *A*–*B* interface (or the active-site interface) between the *A*

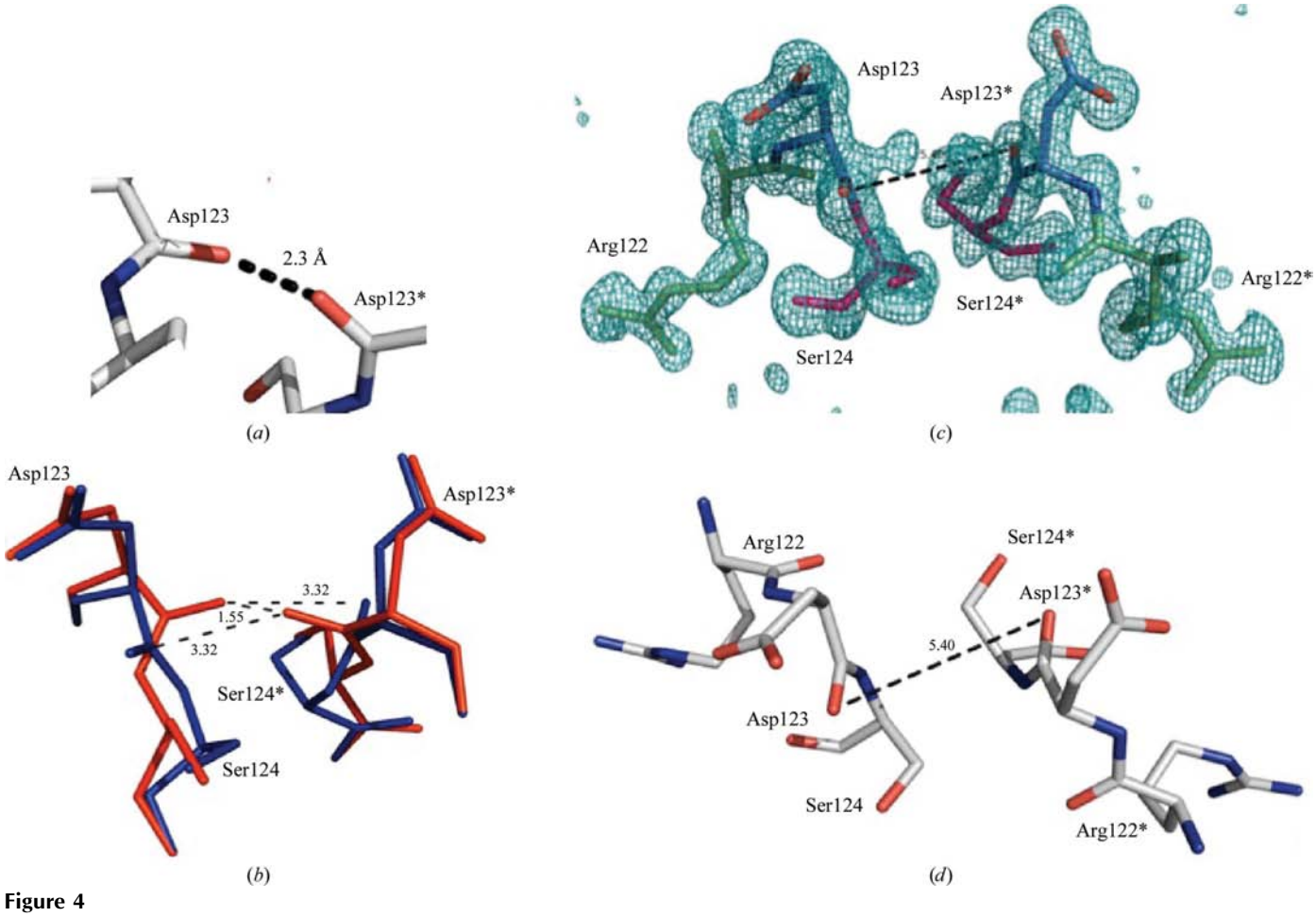

Figure 4
High-resolution UOX–xanthine structure: the rebuilding of the side chain in a twofold crystallographic axis contact region. (*a*) The Asp123–Asp123* contact in the 1ws2 structure. (*b*) The two alternate positions adopted in the 1r4s or 1r51 structures. (*c*, *d*) The rebuilt 122–124 chain in the present high-resolution structure of the UOX–XAN complex. The OMIT map is contoured at the 2.5σ level above the mean.

and *B* or the *C* and *D* monomers, which defines the largest buried surface area (∼6000 Å^2), the *A*–*C* interface (between the *A* and *C* or the *B* and *D* monomers), which also has a large buried surface area (∼5200 Å^2), and the *A*–*D*-type interface (between the *A* and *D* or the *B* and *C* monomers) of smaller size (buried area of ∼800 Å^2) that delimits the access zone of the substrate to the active site.

Since substrate and inhibitor molecules bind at sites located at *A*–*B*-type interfaces, their affinity is tightly related to the interface structure and integrity, as has been demonstrated by a recent pressure-dependent study (Girard *et al.*, 2010).

All of the ligands used (XAN, 8NXN and 8THIO) were observed at the same place within the active site as uric acid (UA). The constitutive elements of the reaction topology are identical in all of the complexes: the Arg176/Gln228 molecular tweezers holds the ligand, the stacked Phe159 is located on one side of the ligand and the peroxo hole, built by the side chains of Asn254 and Thr57* (Figs. 3*b*, 5 and 8*b*), is located on the other side. Two additional hydrogen bonds to amide N atoms (Val227 and Thr57*) and two water molecules W-1 and W-2 (the two ends of the acid–base proton shuttle) complete the binding scheme.

3.1. Atomic resolution structure of the UOX–xanthine complex

In the atomic resolution structure of UOX–XAN, a number of findings that were not fully understood in previous urate oxidase structures have now been assessed thanks to the accuracy of the model. The contact zone between monomers, delimited by residues 122–126, was rebuilt. In all of the room-temperature structures this region displays a very short contact around one of the crystallographic twofold axes of the *I*222 space group between the main-chain O atom of Asp123 and its symmetry mate. In the 2iba structure the O—O* distance is as short as 1.50 Å and in the 1ws2 structure, which contains the full tetramer in the asymmetric unit (space group $P3_121$; 2.70 Å resolution; Retailleau *et al.*, 2005), this distance is around 2.3 Å (Fig. 4*a*). This unusually close contact is always associated with a strong positive residual density located on the twofold axis and the exact situation was not completely analyzed at the time. Several attempts were made to tackle this problem using a residue in two alternate flipped positions for Asp123 (see, for example, the 1r51 and 1r4s structures; Retailleau *et al.*, 2004; Fig. 4*b*). The result was better in terms of electron density, but the contacts remained unsatisfactory. A reinvestigation of this region at 1.0 Å resolution now clearly shows density for the chain that allowed correct rebuilding of the region around Asp123 without any contacts with its symmetry-related equivalent (Fig. 4*c* and 4*d*). Nevertheless, analysis of the Ramachandran plot revealed that a problem is reported for the next residue Ser124, which is pushed out of the low-energy domains of the φ/ψ energy landscape. This unfavourable conformation of Ser124 was attributed to the high strain that is present in the loop. Such strained residues are becoming more and more commonly observed in very high-resolution structures, such as for example the case of a strained threonine (Thr204) in the structure of L-asparaginase (Lubkowski *et al.*, 2003). This new modelled loop was imposed for all UOX structures refined in the present study.

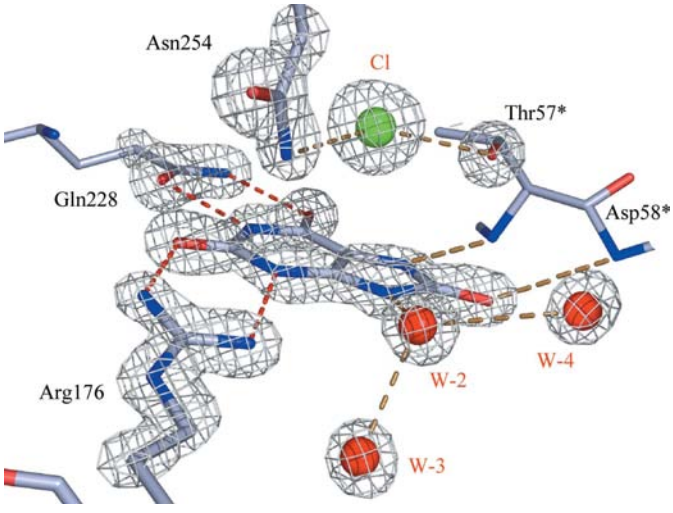

Figure 5
The content of the active site in the UOX–UA structure with a chloride ion in the peroxo hole (OMIT map with calculated phases, contoured at 2.5σ above the mean density).

3.2. UOX–8-nitroxanthine

The halochromic 8-nitroxanthine (8NXN) was initially used in spectroscopic studies because of its particular resonance (Doll *et al.*, 2005). The monoanion displays a bright yellow colour in solution at pH 8, while the dianion turns deep red at highly basic pH (>11). Upon binding to UOX at neutral pH, a dramatic change in colour was observed, suggesting an immediate change in the degree of ionization of 8NXN (Fig. 3*a*). At the resolution to which the crystals of the UOX–8NXN complex diffract, refinement of the structure indicated that the 8NXN molecule is held in the active site in exactly the same way as all of the other inhibitors (Fig. 3*b*).

3.3. UOX–uric acid structure

When a crystal of UOX–8NXN is soaked in a buffered solution of uric acid (UA), ligand exchange occurs readily and catalysis starts immediately by displacement of 8NXN. The reaction can be followed by the crystal colour, which changes from orange/red to pale yellow. To prevent the rapid oxidation of uric acid, it is necessary to slow the reaction, for example by adding sodium chloride to the buffered solution. Under these conditions, release of the product becomes kinetically more rapid compared with substrate binding. Fig. 5 (OMIT map) shows the electron density observed when ∼0.2 *M* NaCl is employed and the reaction is immediately quenched. The peroxo site is found to be occupied by a chloride ion, a clear indication that chloride and oxygen compete for the same site, as mentioned previously (Colloc'h *et al.*, 2008). In the following, the notation UOX–UA–Cl will be used for this complex. In addition to the seven 'standard' polar interactions within the active site, uric acid now makes a new interaction

with the NH of the main chain of Asp58* through its carbonyl group at C8, as previously noted in the UOX–UA structure in complex with cyanide (Gabison *et al.*, 2008).

3.4. UOX–8-thiouric acid structure

8-Thiouric acid (8THIO) has long been recognized as a competitive inhibitor (Bergmann *et al.*, 1962). The structure of 8THIO in complex with UOX is interesting because it leads to a nonproductive complex. 8THIO shares an unsaturated group at C8 with uric acid, which in the case of 8THIO mimics the carbonyl of the natural substrate. However, in the UOX–8THIO structure two molecules of 8THIO are observed, one in the active site and the other engaged in a disulfide bridge with the free and solvent-accessible Cys35, an indication that 8THIO reacts more as a enethiol (or 8-thiolxanthine) tautomer than the thiocarbonyl isomer of 8-thiouric acid. As in the uric acid complex structure, the 8THIO ligand in the active site is held by the seven 'standard' polar interactions plus an interaction with the main-chain NH of Asp58* (Fig. 6*a*). The second molecule of 8THIO is covalently bound to Cys35 (Fig. 6*b*) and is stabilized by six hydrogen bonds, mainly to water molecules, plus an unexpected Tris anion (the buffer employed in crystallization) that was clearly identified in the electron density.

4. Discussion

4.1. The protonation state of the ligand

One of the main objectives of this study was to focus on the immediate environment around the ligand within the active site and to deduce its protonation state from a hydrogen count. The corresponding difference map at 1.0 Å resolution is shown in Fig. 7. The xanthine ligand is held in place by seven polar contacts (here, hydrogen bonds): four to the molecular tweezers (Arg176 and Gln228) plus one to the main chain of Val227 in the same manner as observed for all other inhibitors/substrates. The two other polar interactions are with the water molecule W-2 and the N—H main-chain atoms of Thr57*. At the pH of the reaction, xanthine, with a pK_a of 7.53, should be in the monoanionic form and should have three H atoms, but only two emerge easily from the map: the C(8)—H atom and to a lesser extent, the N(1)—H atom. The two other H atoms are not observed on either N(3) nor N(9), an indication that xanthine is certainly in a higher ionization state (double). At the pH of crystallization Arg176 is protonated, so ionization of N(3) was expected. The ionization of N(9) remains uncertain but is strongly supported by the complexes with urate and the halochromic inhibitor 8NXN.

In the UOX–UA–Cl complex and at pH 8 uric acid is monodeprotonated before entering the active site (pK_1 = 5.4, pK_2 = 10.3). Once complexed, the count of protons around uric acid favours double deprotonation, if we consider the donor/acceptor status of all interactions around the substrate. As in the case of xanthine, two H atoms of UA cannot be present on N(3) and N(7) because these two N atoms face other hydrogen-donor N atoms. A similar conclusion of double deprotonation of the substrate can also be drawn for the UOX–8NXN complex owing to the colour change on ligand binding.

From all these convergent observations, two possibilities emerge regarding the ionization state of the substrate: it could be either a dianion or a radical monoanion, both of which have the same count of protons.

In regard to the first case, the dianion is considered to be very reactive but a mystery still remains as it stays in a quantum singlet state that is not able to react directly with dioxygen.

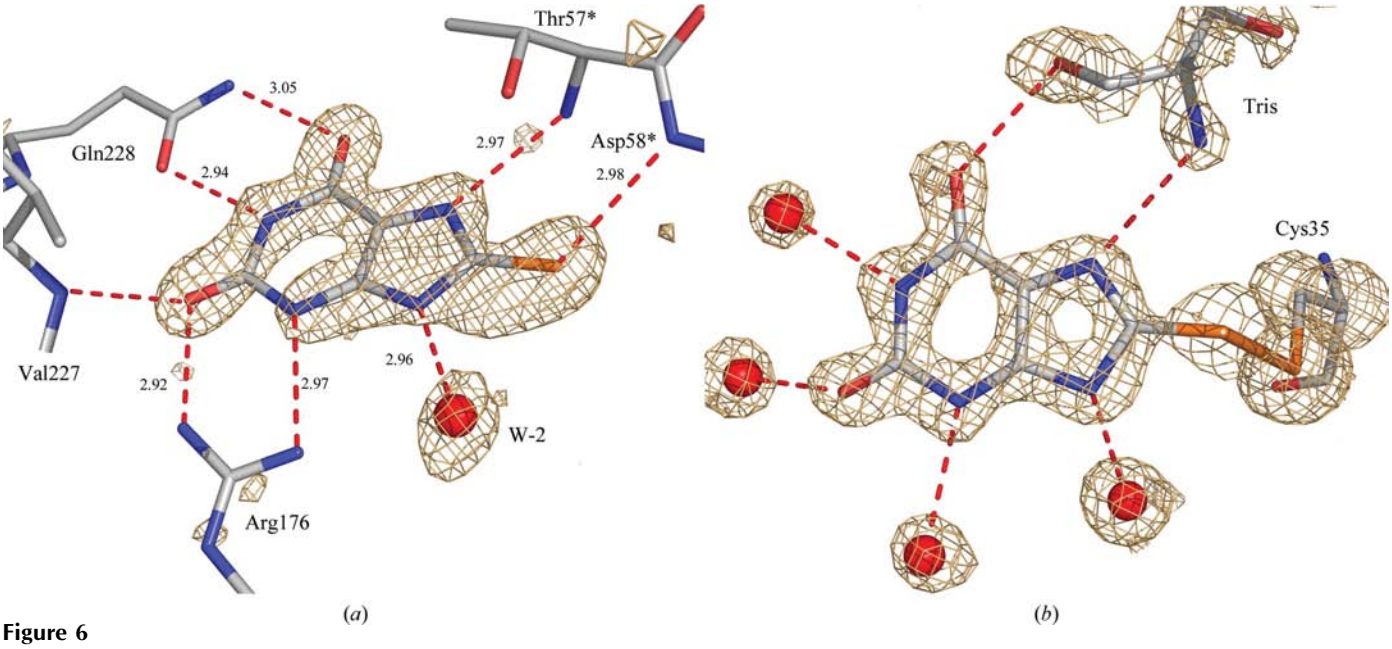

Figure 6
UOX–(8THIO)$_2$ structure. (*a*) The active-site content. (*b*) The second 8THIO bridged to Cys35 as a disulfide thioenol. OMIT maps contoured at the 2.5σ level.

Concerning the second case, a recent paper (Busi *et al.*, 2007) revealed some important information by showing that the UOX reaction gives a strong signal in EPR spectroscopy. This signal was attributed to arise from a hypothetical 4-hydroxyisourate radical. Although not firmly proven, this intermediate gives credit to a monoelectron pathway for the reaction; it favours the radical monoanion of uric acid being the true starting intermediate instead of the dianion. Again, how this putative radical is so easily produced by UOX remains to be documented experimentally.

4.2. The general base catalytic system

The deprotonation of the urate monoanion in the first step of the reaction was indicated by Tipton and coworkers to be crucial in the enzymatic mechanism. These authors advocated the dyad Lys10–Thr57 to be the putative general catalytic base that is responsible for the rapid proton elimination leading to a reactive dianion of uric acid at the beginning of catalysis (Imhoff *et al.*, 2003), based on the initial X-ray structure of UOX (Colloc'h *et al.*, 1997). However, in all of the X-ray structures determined to date (Retailleau *et al.*, 2004, 2005; Gabison *et al.*, 2006, 2008), a pair of structurally well conserved water molecules are observed within the active site around the ligand that could be good candidates to play the role of acid–base system terminators: W-1 is located in the peroxo hole and W-2 is always present in the mean plane of the ligand and is strongly hydrogen bonded to the N(9) atom of the substrate. There are two exceptions. (i) In the monoclinic structure of native UOX (PDB code 1r56), the eight independent active sites of which were empty, the side chains of Asn254 above the active-site location are loosely oriented and do not face Thr57* in building the peroxo hole; W-1 is thus absent in four of the eight independent active sites. (ii) In the 9-methyluric acid complex (PDB code 1r4s) the 9-methyl group of the ligand prevents W-2 from being present.

These water molecules display all the characteristics of two end points of an efficient acid–base system that is able to

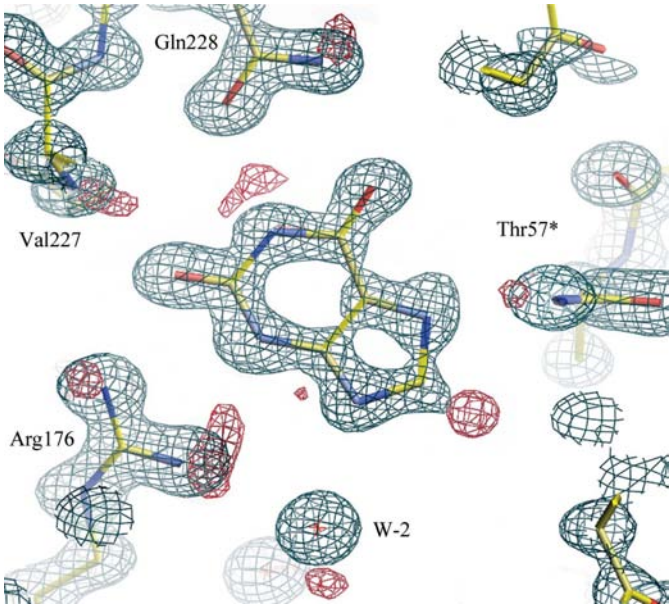

Figure 7
The protonation state of xanthine bound in the active site. The $2mF_o - DF_c$ (σ map, contoured at 3σ) map calculated before the last cycle is shown in blue; the $F_o - F_c$ map showing the location of H atoms (contoured at 2.5σ) is shown in red.

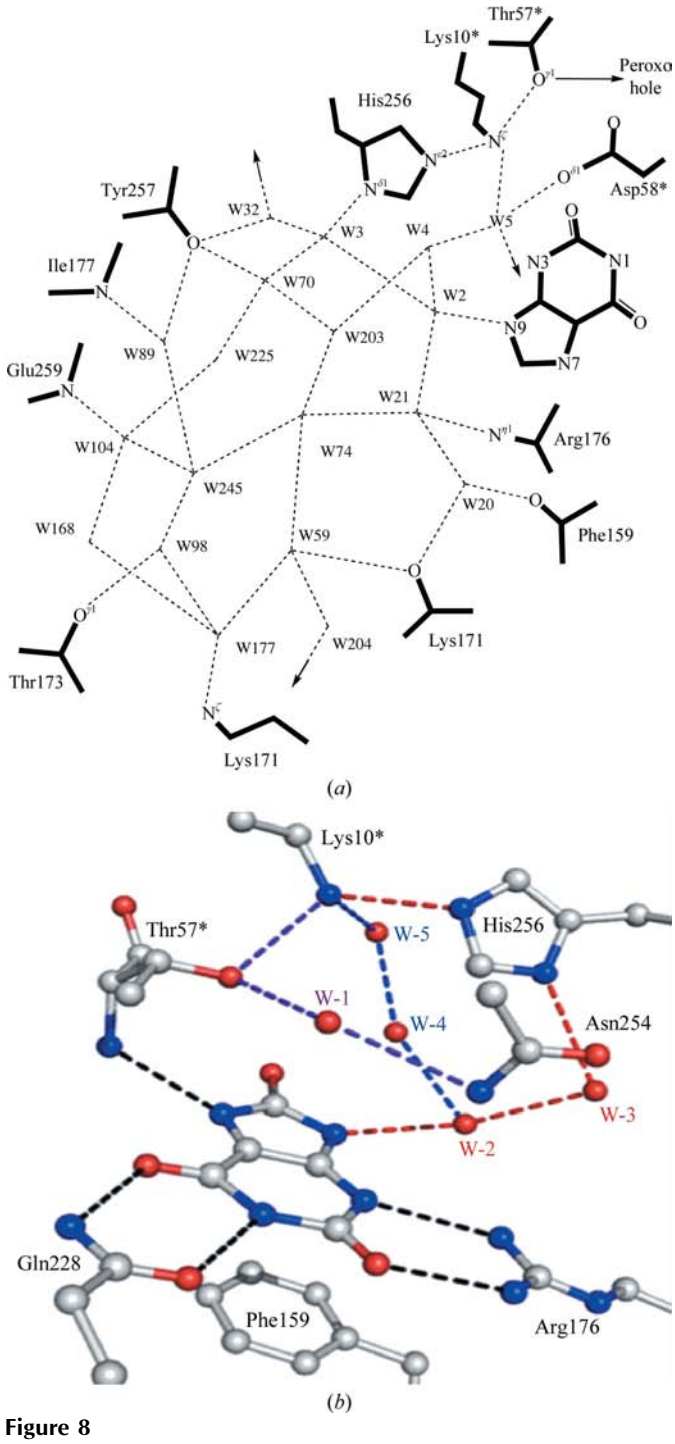

Figure 8
(*a*) Schematic drawing of the hydrogen-bond network starting from the N(9) atom of the uric acid/xanthine ligand that is able to form an efficient proton buffer. (*b*) The two parallel acid–base networks (or proton shuttle) for proton transfer between N(9) and the peroxo hole (the main network including the triad His256–Lys10*–Thr57* and W-3 is shown in blue; the alternate network with W-4 and W-5, bypassing the histidine residue, is shown in red).

transfer a proton, according to their connection to a large and extended network of polar side chains/water molecules that is best described in the UOX–XAN structure (Fig. 8). This network involves more than 20 structural water molecules and several polar atoms of the protein; it extends over the two subunits forming the active site (Fig. 8*a*). All of these molecules have low temperature factors, with three or four of their four polar contacts involved in polygonal motifs and as such able to play the role of a low-energy proton buffer. This proton buffer is connected to the N(9) atom of the substrate by W-2 and to the catalytic peroxo hole by W-1; these connections imply two parallel networks as shown in Fig. 8(*b*). The first branch includes the previously described catalytic Thr–Lys dyad (Imhoff *et al.*, 2003) plus His256 as a proton relay (the dyad is now extended as a triad) and W-3. The second alternative network bypasses His256; it implies that W-2, W-4 and W-5 connect N(9) directly to Lys10* and would explain why His256 is not strictly conserved in urate oxidases, in contrast to Lys10 and Thr57. These two connections are observed in all of the structures of UOX–inhibitor complexes, except when the peroxo hole contains a repulsive (negatively charged) cyanide ion, in which case the link between Thr57* and Lys10* is broken (Gabison *et al.*, 2008).

4.3. UOX–XAN: how far can we go regarding hydrogen information?

Determining H-atom locations from X-ray structures is worthy of note and the present paper should include some information about the limits and drawbacks of high-resolution X-ray crystallography (*i.e.* at ∼1 Å) in its ability to obtain accurate data about H atoms. In this context, the development of refinement software has been one of the most useful tools, starting with the seminal *PROLSQ* (Konnert & Hendrickson, 1980) and *CORELS* (Sussman, 1985) programs that worked at low and moderately high resolution (∼1.7 Å), followed by the emergence of *REFMAC* (Murshudov *et al.*, 1997; Skubák *et al.*, 2004), *TNT* (Tronrud, 1997), *SHELXL* (Sheldrick, 2008) and *BUSTER-TNT* (Blanc *et al.*, 2004), which allowed convenient and comfortable application at high resolution by including anisotropic description of atoms and, for some of them, information about experimental phases or more sophisticated treatment of incomplete models. Recently, Lecomte and coworkers have developed *MoPro* for use at ultrahigh resolution by also including bond densities and lone-pair contributions in the model (Jelsch *et al.*, 2005), with a number of successes, particularly in the case of aldol reductase (Podjarny *et al.*, 2001; Howard *et al.*, 2004), and also for several other proteins (Housset *et al.*, 2000; Jelsch *et al.*, 2000; Afonine *et al.*, 2004). However, ultrahigh resolution in macromolecular crystallography is far from being the rule, even if the use of data at resolution better than 0.7 Å makes the treatment of H atoms a trivial task that is comparable in some ways to neutron crystallography (Blakeley *et al.*, 2006). In the case of 'normal'

Table 2
Statistics and distribution of hydrogen recovery, according to the average recalculated isotropic thermal factor of the residue.

Average ⟨*B*⟩ factor (Å^2)	5–11 (low)	11–18 (medium)	18+ (high)
No. of residues	82	146	67
H recovery (%)			
In main chain	78	55	44
In side chains	55	30	15

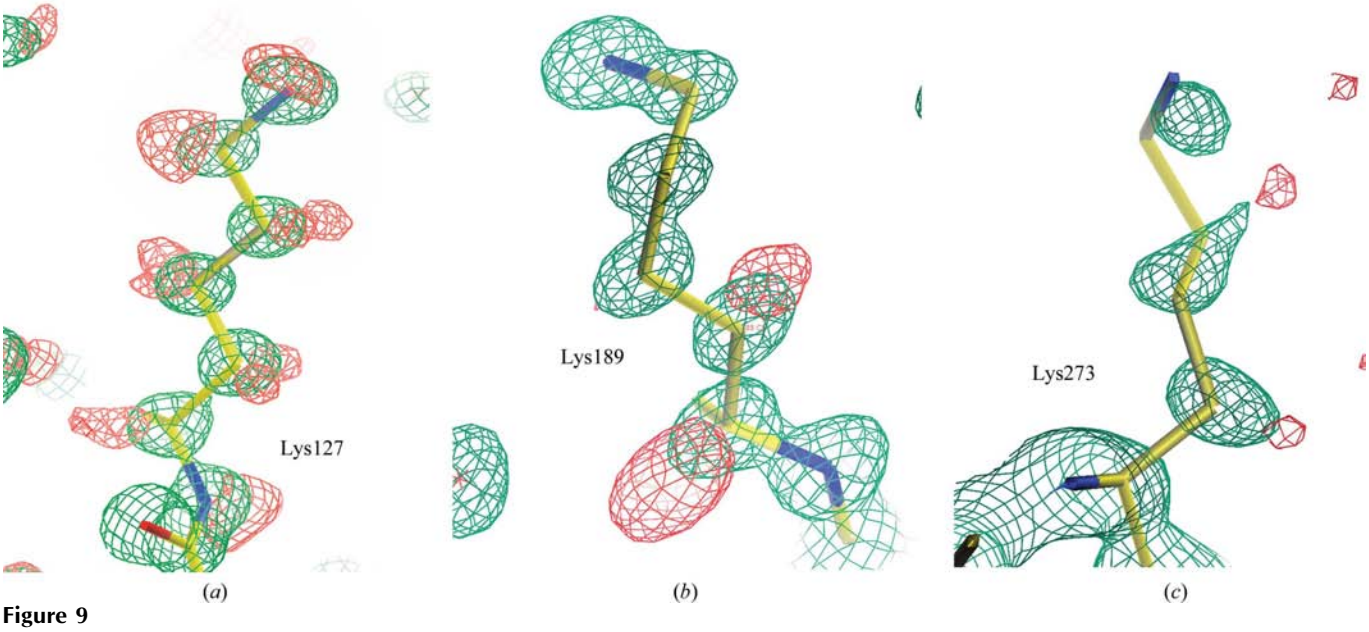

Figure 9
UOX–XAN structure. Different hydrogen-omit maps for several lysine residues. (*a*) A 'good' case (Lys127); most of the H atoms can be observed (except for those of the terminal N$^{\zeta}$ atom). (*b*) The moderately agitated Lys189: only the densities corresponding to H$^{\alpha}$, H$^{\beta}$ and, to a lesser extent, H$^{\gamma}$ emerge. (*c*) The highly agitated Lys273, where only two low densities are observed. Green, $2F_o - F_c$ maps contoured at 2.5σ above the mean (except for Lys273, which is contoured at 1.7σ). Red, H-omit maps contoured at 2.5σ.

high resolution, say between 1.2 and 1 Å, the technique becomes questionable and has triggered a number of discussions about the exploitation of experimental results (Dauter *et al.*, 1997; Dauter, 2003; Jelsch *et al.*, 2005; Ahmed *et al.*, 2007).

In this context, one may consider two main different situations regarding the location of H atoms, in addition to the characteristics that have been extensively reviewed by Ahmed *et al.* (2007).

The first addresses the *B* factor of the bearing atom and the second the type of bond, as hydrogen may be involved either in a strong σ C—H bond or in a less 'visible' bond that can be either a rotating C—H bond (methyl groups) or an exchangeable O—H or N—H bond.

In the first case, thermal agitation is the main factor that prevents hydrogen location. It is well known that Debye–Waller factors are strongly correlated not only with thermal agitation but also with crystal quality, mosaicity, resolution, local and long-distance disorder and defects that may appear during the crystallization process. Cooling the crystal to liquid-nitrogen temperature usually results in a decrease in the average values of *B* factors but conversely induces an increase in crystal defects because of the shock during annealing and ice expansion. This situation can be overcome by some ingenious processes (Kim *et al.*, 2005) but these are somewhat difficult to set up in routine experiments. Overall, the balance between these beneficial and destructive effects usually leads to an improvement of the resolution in the majority of cases.

In the second case, when H atoms are connected to C atoms the situation is far better than when they are linked to oxygen (as in serine, threonine or tyrosine) or nitrogen (as in lysine, arginine *etc.*). Even the amide H atoms of the main chain may be somewhat difficult to observe.

To tackle all these situations, the residues in the UOX–XAN complex structure were ranked by their average $\langle B \rangle$ factors into three groups: low, medium and high, with arbitrary limits fixed at 11 and 18 Å^2. In each class, the percentage of H atoms observed in difference maps using refined phases were calculated and are reported in Table 2. An illustration is given (Fig. 9) using the lysine side chain as a probe; this residue is known to be sensitive to agitation and is very often a nightmare in refinement because most of the time the chain is dangling at the protein surface with little interaction (the same also holds for arginine residues). The UOX monomer contains 23 lysine residues, most of which are located at the surface. One lysine was selected from each bin: (i) Lys127 with a low $\langle B \rangle$ of 9.5 Å^2, (ii) Lys189 with a medium $\langle B \rangle$ of 15.6 Å^2 and (iii) Lys273 with a high $\langle B \rangle$ of 39 Å^2. In the first case most of the H atoms emerged from hydrogen-omit maps, while in the second case only the C$^{\alpha}$ and C$^{\beta}$ H atoms were observed. In the last case, only two small extensions of densities were observed along the chain. In all cases, the H atoms at the N$^{\zeta}$ end were not observed at the 2σ level that we selected in maps. The pathologically disordered lysines at the surface of the protein, *i.e.* Lys4, Lys23, Lys114, Lys138 and Lys171, that were treated as multi-position groups were not considered. In this case even at a resolution of 1.0 Å searching for H atoms becomes hopeless.

5. Conclusions

The aim of this paper was to exploit the high-resolution structures of urate oxidase–inhibitor complexes to evaluate the protonation state of uric acid in the early stage of the reaction. The work here reports the structure of a xanthine complex at 1 Å resolution, from which information about H atoms can be derived as long as they are in static locations. We confirmed the presence of two H atoms on the ligand, but could only suggest that a third hydrogen on the N(9) atom would be absent. This structure illustrates some of the limitations of the X-ray diffraction method in showing protonation/deprotonation sites. Three other complex structures at near-atomic resolution (*i.e.* in the resolution range 1.3–1.7 Å) helped us to ascertain that the substrate is in a higher ionization state, particularly by the use of a halochromic inhibitor (8-nitroxanthine). All of these UOX–ligand structures particularly highlight the role of a large network connecting the N(9) atom of the ligand to the peroxo hole and suggest a well conserved structural motif for proton transfer (a proton shuttle or an acid–base system). Nevertheless, how the enzyme generates the substrate as a suitable reactive monoelectron species from the dianion and how the enzyme can manage to bypass the restriction imposed by the spin rule without any aid from a metal or a cofactor still remain to be described.

This work was supported by CNRS, Université Paris Descartes and Université de Caen Basse-Normandie and by a grant from the Ministère de l'Education Nationale et de la Recherche (to LG). We would like to thank Hassan Belhrali, Martin Walsh (BM14), Jean-Luc Ferrer and Michel Pirocchi (BM30 or FIP), and Ana Labrador and Randolf Butzbach (BM16) for advice at the ESRF beamlines, Grenoble, France.

References

Afonine, P. V., Lunin, V. Y., Muzet, N. & Urzhumtsev, A. (2004). *Acta Cryst.* D**60**, 260–274.
Ahmed, H. U., Blakeley, M. P., Cianci, M., Cruickshank, D. W. J., Hubbard, J. A. & Helliwell, J. R. (2007). *Acta Cryst.* D**63**, 906–922.
Altarsha, M., Castro, B. & Monard, G. (2009). *Bioorg. Chem.* **37**, 111–125.
Bergmann, F., Ungar-Waron, H. & Kwietny-Govrin, H. (1962). *Biochem. J.* **86**, 292–298.
Blakeley, M. P., Mitschler, A., Hazemann, I., Meilleur, F., Myles, D. A. & Podjarny, A. (2006). *Eur. Biophys. J.* **35**, 577–583.
Blanc, E., Roversi, P., Vonrhein, C., Flensburg, C., Lea, S. M. & Bricogne, G. (2004). *Acta Cryst.* D**60**, 2210–2221.
Brünger, A. T., Adams, P. D., Clore, G. M., DeLano, W. L., Gros, P., Grosse-Kunstleve, R. W., Jiang, J.-S., Kuszewski, J., Nilges, M., Pannu, N. S., Read, R. J., Rice, L. M., Simonson, T. & Warren, G. L. (1998). *Acta Cryst.* D**54**, 905–921.
Busi, E., Sinicropi, A., Terzuoli, L., Marinello, E. & Basoso, R. (2007). *Appl. Magn. Reson.* **31**, 471–482.
Chen, V. B., Arendall, W. B., Headd, J. J., Keedy, D. A., Immormino, R. M., Kapral, G. J., Murray, L. W., Richardson, J. S. & Richardson, D. C. (2010). *Acta Cryst.* D**66**, 12–21.
Collaborative Computational Project, Number 4 (1994). *Acta Cryst.* D**50**, 760–763.

Colloc'h, N., el Hajji, M., Bachet, B., L'Hermite, G., Schiltz, M., Prangé, T., Castro, B. & Mornon, J. P. (1997). *Nature Struct. Biol.* **4**, 947–952.
Colloc'h, N., Gabison, L., Monard, G., Altharsha, M., Chiadmi, M., Marassio, G., Sopkova-de Olivera Santos, J., El Hajji, M., Castro, B., Abraini, J. & Prangé, T. (2008). *Biophys. J.* **95**, 2415–2422.
Colloc'h, N., Sopkova-de Oliveira Santos, J., Retailleau, P., Vivarès, D., Bonneté, F., Langlois d'Estainto, B., Gallois, B., Brisson, A., Risso, J.-J., Lemaire, M., Prangé, T. & Abraini, J. H. (2007). *Biophys. J.* **92**, 217-224.
Dauter, Z. (2003). *Methods Enzymol.* **368**, 288–337.
Dauter, Z., Lamzin, V. S. & Wilson, K. S. (1997). *Curr. Opin. Struct. Biol.* **7**, 681–688.
Doll, C., Bell, A. F., Power, N., Tonge, P. J. & Tipton, P. A. (2005). *Biochemistry*, **44**, 11440–11446.
Fetzner, S. (2002). *Appl. Microbiol. Biotechnol.* **60**, 243–257.
Fetzner, S. & Steiner, R. (2010). *Appl. Microbiol. Biotechnol.* **86**, 791–804.
Gabison, L., Chiadmi, M., Colloc'h, N., Castro, B., El Hajji, M. & Prangé, T. (2006). *FEBS Lett.* **580**, 2087–2091.
Gabison, L., Prangé, T., Colloc'h, N., El Hajji, M., Castro, B. & Chiadmi, M. (2008). *BMC Struct. Biol.* **8**, 32.
Girard, É. *et al.* (2010). In the press.
Konnert, J. H. & Hendrickson, W. A. (1980). *Acta Cryst.* A**36**, 344–350.
Housset, D., Benabicha, F., Pichon-Pesme, V., Jelsch, C., Maierhofer, A., David, S., Fontecilla-Camps, J. C. & Lecomte, C. (2000). *Acta Cryst.* D**56**, 151–160.
Howard, E. I., Sanishvili, R., Cachau, R. E., Mitschler, A., Chevrier, B., Barth, P., Lamour, V., Van Zandt, M., Sibley, E., Bon, C., Moras, D., Schneider, T. R., Joachimiak, A. & Podjarny, A. (2004). *Proteins*, **55**, 792–804.
Imhoff, R. D., Power, N. P., Borrok, M. J. & Tipton, P. A. (2003). *Biochemistry*, **42**, 4094–4100.
Jelsch, C., Guillot, B., Lagoutte, A. & Lecomte, C. (2005). *J. Appl. Cryst.* **38**, 38–54.
Jelsch, C., Teeter, M., Lamzin, V., Pichin-Pesme, V., Blessing, R. H. & Lecomte, C. (2000). *Proc. Natl Acad. Sci. USA*, **97**, 3171–3176.
Kahn, K. & Tipton, P. A. (1997). *Biochemistry*, **36**, 4731–4738.
Kim, C. U., Kapfer, R. & Gruner, S. M. (2005). *Acta Cryst.* D**61**, 881–890.
Laskowski, R. A., MacArthur, M. W., Moss, D. S. & Thornton, J. M. (1993). *J. Appl. Cryst.* **26**, 283–291.
Leslie, A. G. W. (1992). *Jnt CCP4/ESF–EACBM Newsl. Protein Crystallogr.* **26**.
Loo, T., Michael, M. E., Garceau, A. J. & Reid, J. C. (1959). *J. Am. Chem. Soc.* **81**, 3039–3041.
Lubkowski, J., Dauter, M., Aghaiypour, K., Wlodawer, A. & Dauter, Z. (2003). *Acta Cryst.* D**59**, 84–92.
Mosselhi, M. A. & Pfleiderer, W. (1993). *J. Heterocycl. Chem.* **30**, 1221–1228.
Murshudov, G. N., Vagin, A. A. & Dodson, E. J. (1997). *Acta Cryst.* D**53**, 240–255.
Otwinowski, Z. & Minor, W. (1997). *Methods Enzymol.* **276**, 307–326.
Perrakis, A., Harkiolaki, M., Wilson, K. S. & Lamzin, V. S. (2001). *Acta Cryst.* D**57**, 1445–1450.
Podjarny, A., Howard, E. I., Mitschler, A., Chevrier, B., Lecomte, C., Guillot, B. & Jelsch, C. (2001). *Bull. Soc. Fr. Phys.* **131**, 12–15.
Ramazzina, I., Folli, C., Secchi, A., Berni, R. & Percudani, R. (2006). *Nature Chem. Biol.* **2**, 144–148.
Retailleau, P., Colloc'h, N., Vivarès, D., Bonneté, F., Castro, B., El Hajji, M., Mornon, J.-P., Monard, G. & Prangé, T. (2004). *Acta Cryst.* D**60**, 453–462.
Retailleau, P., Colloc'h, N., Vivarès, D., Bonneté, F., Castro, B., El Hajji, M. & Prangé, T. (2005). *Acta Cryst.* D**61**, 218–229.
Sheldrick, G. M. (2008). *Acta Cryst.* A**64**, 112–122.
Skubák, P., Murshudov, G. N. & Pannu, N. S. (2004). *Acta Cryst.* D**60**, 2196–2201.
Sussman, J. L. (1985). *Methods Enzymol.* **115**, 271–303.
Tipton, P. A. (2002). *Methods Enzymol.* **354**, 310–319.
Tronrud, D. E. (1997). *Methods Enzymol.* **227**, 306–319.